Dual Discontinuous PWM-Based Power Distribution Control of Multisource Inverters

Dehong Zhou, *Senior Member, IEEE*, Zhao Zhang, *Student Member, IEEE*, Xin Liu, *Member, IEEE*, Zewei Shen, *Member, IEEE*, and Jianxiao Zou, *Member, IEEE*

***Abstract*—The multisource inverter (MSI) is a promising topology for hybrid electric vehicles due to its advanced merits of single-stage power conversion from each source to the motor without dc–dc converters. However, it is challenging to design a modulation scheme for the MSI since it not only determines the output voltage on the ac side, but also the power distribution between the sources on the dc side. Furthermore, the computation burden for the MSI is heavy due to its unsymmetrical distributed voltage vectors. Given this, this article proposes a dual discontinuous pulsewidth modulation (D^2PWM) scheme to simultaneously realize power distribution and motor drive control for the MSI. In the proposed D^2PWM, the MSI is decomposed into two independent subinverters, and modulation schemes of each subinverter can be implemented in symmetric space-vector diagrams, which avoids heavy computational burden under the unsymmetrical voltage vector diagram. Besides, the total switching times of 3 in the proposed D^2PWM are realized by assigning the desired voltage vector for one of the subinverters aligned with the basic voltage vectors, which reduces the switching losses in this decomposed model and improves the current quality of the MSI. Comparative experimental results confirm the effectiveness of the proposed D^2PWM.**

***Index Terms*—Discontinuous pulsewidth modulation (DPWM), hybrid electric vehicle, multisource inverter, permanent-magnet synchronous motor (PMSM), single-stage conversion.**

Manuscript received 19 October 2023; revised 7 January 2024, 26 February 2024, and 21 April 2024; accepted 17 May 2024. Date of publication 21 May 2024; date of current version 16 July 2024. This work was supported in part by the National Natural Science Foundation of China under Grant 62173067, in part by the Guangdong Basic and Applied Basic Research Foundation under Grant 2024A1515010184 and Grant 2023A1515240060, in part by Guangdong Science and Technology Program under Grant 2021QN02L854, in part by Sichuan Science and Technology Program under Grant 2023NSFSC0298, and in part by the Shenzhen Science and Technology Program under Grant JCYJ20220530165001003, Grant JCYJ20230807120006012, and Grant JSGG20220831110805010. Recommended for publication by Associate Editor G. Konstantinou. *(Corresponding author: Dehong Zhou.)*

Dehong Zhou and Jianxiao Zou are with the School of Automation Engineering, University of Electronic Science and Technology of China, Chengdu 611731, China, and also with the Shenzhen Institute for Advance Study, University of Electronic Science and Technology of China, Shenzhen 518000, China (e-mail: dhzhou@uestc.edu.cn; jxzou@uestc.edu.cn).

Zhao Zhang is with the School of Automation Engineering, University of Electronic Science and Technology of China, Chengdu 611731, China (e-mail: 202222280546@std.uestc.edu.cn).

Xin Liu is with the Shenzhen Institute for Advanced Study, University of Electronic Science and Technology of China, Shenzhen 518000, China (e-mail: liu_xin@uestc.edu.cn).

Zewei Shen is with the School of Automation Engineering, University of Electronic Science and Technology of China, Chengdu 611731, China, and also with the Shenzhen Institute for Advance Study, UESTC, Shenzhen 518000, China (e-mail: shenzw@uestc.edu.cn).

Color versions of one or more figures in this article are available at https://doi.org/10.1109/TPEL.2024.3403881.

Digital Object Identifier 10.1109/TPEL.2024.3403881

I. Introduction

ELETRIC vehicles (EVs) are considered a viable solution to deal with fossil fuel depletion and environmental problems [1]. As a mature technology, Li-ion batteries have been widely used as primary energy storage systems of commercially available EVs. However, Li-ion batteries have limitations, such as limited power density, low charge/discharge lifespan, and poor operation in cold temperatures. Energy source hybridization-based hybrid EVs (HEVs) combining the power output of two or more energy sources with complementary characteristics becomes a preferred choice due to their advanced features in terms of initial investment, efficiency, source lifespan, reliability, and system redundancy [2], [3], [4], [5].

The multisource inverter (MSI) is an attractive solution for integrating multiple energy sources in the HEV applications [6], [7], [8], [9], [10]. Its essential purpose is to connect several dc sources to the same ac output using a single conversion stage. Fig. 1 depicts the topology with ideal switches. As shown, the MSI provides two dc terminals and one ac terminal, where two dc sources, namely v_L and v_H, are connected to two dc terminals, while the motor is connected to the ac terminal. This type of inverter enables direct power delivery between the motor and the energy sources without employing dc–dc converters, featuring advanced merits of single-stage power conversion, simple configuration, low cost, and easy implementation [11]. Besides, due to the removal of dc–dc converters with their bulky passive filters and capacitors, the power density of the whole system is also substantially increased [12].

Although the above merits of MSI are presented, it is also challenging to design controllers to achieve satisfactory performance for this inverter because the dc port voltages are variable with the state of charge (SoC) of the energy source [13], and the power distribution control should be achieved simultaneously in addition to stator current control. In recent years, substantial research efforts have been conducted regarding the controller design for the MSI. A control scheme beyond the specific PWM modulation [14] was proposed for the power distribution of the MSI. An extra proportional integer (PI) loop is introduced to manage the power distribution between the dc sources. Precise models between port power and zero-sequence component were built in [15], [16], and [17], and direct model-based controllers were proposed for the power distribution between the dc sources. An additional proportional-integral controller was employed for power flow control in the MSI by regulating the injected zero-sequence component to achieve power distribution of the

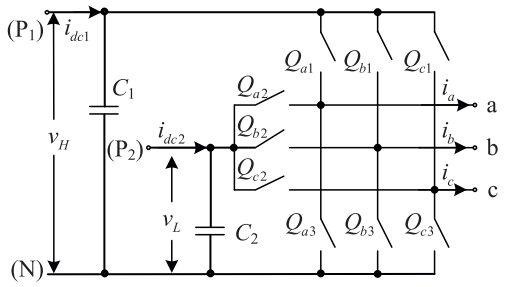

Fig. 1. Configuration of MSI circuit with ideal switches.

sources [18]. The power distribution model, together with active and reactive power control models, was built as a multiobjective control issue in [19], and a model predictive control scheme was presented to achieve these control objectives. In [20], the MSI was modeled as three distinct modes by conducting parts of the semiconductors. The power distribution between the sources is achieved by selecting the operation modes. In [21], a modulated model predictive control strategy was proposed to address the nonlinear and multiobjective characteristics of power distribution in MSI. Although these strategies can realize the power distribution between the sources to some extent, introducing the extra control loops generally has complex structures, slow dynamic response, and complicated control parameter tuning processes.

In view of this, several research efforts were conducted by designing specific modulation schemes to deal with the variable dc-link voltage and the power distribution between the sources in the MSIs. A pulsewidth modulation (PWM) scheme was investigated in [22] by calculating the voltage-second balance equations to generate high-quality output voltage and maximize the linear modulation range. To suppress the common-mode voltage and achieve superior output current quality, a carrier-based modulation scheme is introduced for MSI under unbalanced neutral-point voltage conditions [23]. A hybrid PWM strategy composed of carried-based PWM and discontinuous PWM is proposed to generate high-quality ac voltage [24]. A modified space-vector modulation with coordination projection under the unbalanced dc-link was proposed to optimize the system efficiency [25]. A two-stage modulation scheme was adopted in [26] to maximize the output power of one port through zero-sequence minimization. A dynamic-space-vector DPWM was introduced for addressing unbalanced neutral point voltage with high efficiency and low current THD [27]. To suppress output harmonic and maximize the linear modulation region, a discontinuous SVPWM is investigated in [28]. Although these methods effectively guarantee the output voltage quality under the unbalanced dc-link voltage and achieve power distribution in some fixed operation points, flexible power distribution between the dc sources was unavailable in these works.

Regarding the flexible power distribution control of the MSI, several modulation schemes have been developed recently. A virtual space-vector PWM-based flexible power control was proposed in [29], where power distribution between each port was regulated by adjusting the proportion of the positive and negative small vectors. However, the magnitude of positive and negative small vectors was not equal under unbalanced dc-link voltage, and adjusting the proportion of these vectors would affect the active voltage vector synthesis and deteriorate the motor drive control performance. A vector space decomposition-based modulation scheme was proposed to avoid the heavy computational burden under unsymmetrical space vector diagram [30]. However, this simplification introduced extra switching losses with increased switching times in each control period. Multiple carriers modulation-based PWM scheme was proposed in [31], where the power distribution range could be extended somewhat at the expense of the switching losses. It should be noted that these methods achieve power distribution control of the MSI by indirectly regulating the proportion of redundant voltage vectors or zero-sequence components, which are complicated and not intuitive and bring challenges for power distribution capability analysis and maximum power distribution exploration of the MSI in variable operation points.

In view of this, this article proposes a dual discontinuous PWM (D^2PWM) scheme to simultaneously realize power distribution and motor drive control for the MSI. In the proposed D^2PWM scheme, the MSI is modeled as two independent subinverters, and modulation schemes of each subinverter can be implemented in symmetric space-vector diagrams. As a result, the complicated sector identification and dwell time calculation under the unevenly distributed voltage vector diagram are avoided, and the switching losses can be reduced due to the employment of the discontinuous PWM scheme. Besides, the total switching times of 3 are realized by assigning the desired voltage vector for one of the subinverters aligned with the basic voltage vectors, which reduces the switching losses in this decomposed model and improves the current quality of the MSI. The implementation details of the proposed D^2PWM scheme are analytically presented in this article. A direct power model for the power distribution of MSI is proposed to achieve fast power distribution control and ease the power distribution capability analysis. Experimental tests verify the effectiveness of the proposed scheme.

The rest of the article is organized as follows. Section II presents the system topology and system modeling of the MSI. The D^2PWM-based power distribution control of the MSI is proposed in Section III. The effectiveness of the proposed scheme is experimentally evaluated in Section IV. Finally, Section V concludes the article.

II. Mathematical Model of MSI-Fed Motor Drive

This section introduces the topology of the MSI first. Then, the decomposition model and the constraints for the high-efficiency modulation scheme design of the MSI are presented.

A. Topology of MSI

Fig. 2 illustrates a typical topology for the MSI-based HEVs. For simplicity, a mature topology known as a neutral-point-clamped (NPC) inverter is adopted as an MSI by connecting energy sources to the dc ports directly [14]. The high-voltage port is connected to the primary source, and the low-voltage port is connected to the secondary source. Unlike a traditional

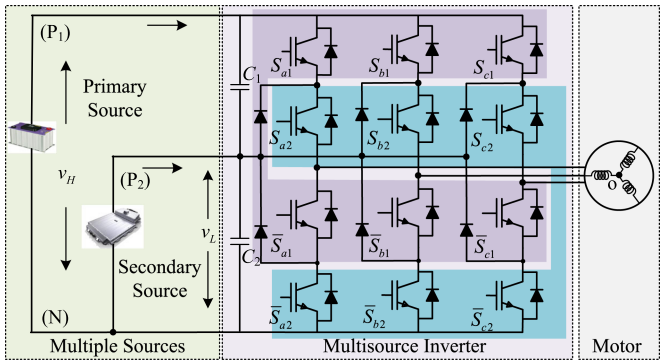

Fig. 2. Topology of an MSI.

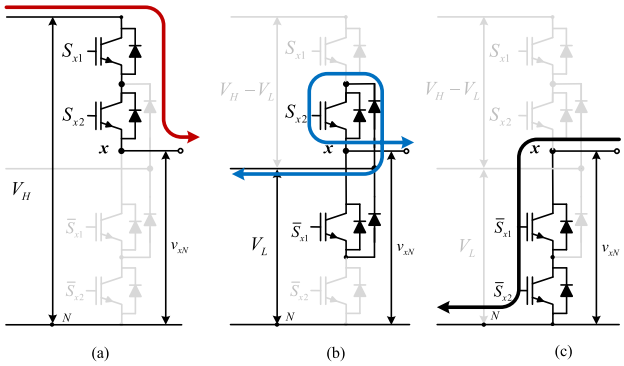

Fig. 3. Current path of MSI.

TABLE I
SWITCHING STATES OF MSI

Gating Signals (S_{x1}, S_{x2})	Output voltage v_{xN}	Switching state S_x	Power source
(1,1)	v_H	2	Primary source
(0,1)	v_L	1	Secondary source
(0,0)	0	0	None of the sources

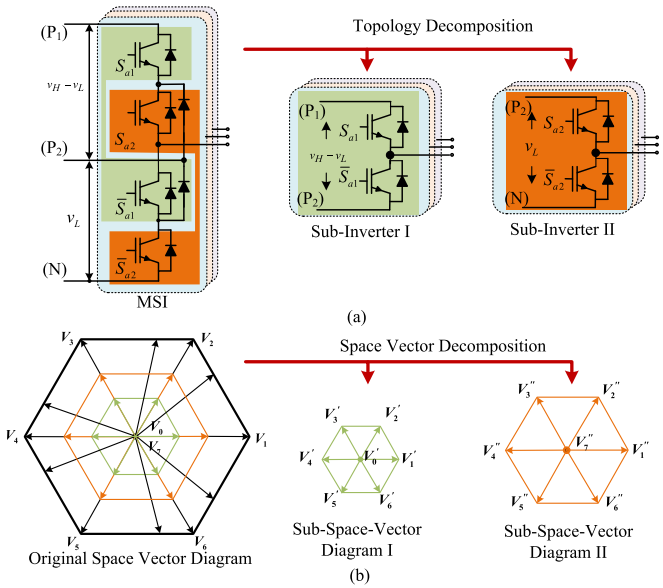

Fig. 4. Topology and space vector diagram decomposition.

NPC inverter, there is no neutral point in the MSI. Therefore, the modulation and control schemes cannot be transplanted directly from the NPC inverter. Both sources are connected to the motor directly, enabling single-stage power conversion from sources to the motor. The permanent-magnet synchronous motor (PMSM), mainly used in EVs because of its high efficiency and compactness, is employed for the MSI investigation.

In each phase of the MSI, it consists of four active switches $S_{x1}, S_{x2}, \bar{S}_{x1}$, and $\bar{S}_{x2}$, $(x \in \{a, b, c\})$ and two diodes, where $\bar{S}_{x1}$ and $\bar{S}_{x2}$ are complementary switching states of S_{x1}, S_{x2}, respectively. It means that when S_{x1} turn ON, $\bar{S}_{x1}$ must be turned OFF, and when S_{x2} turn ON, $\bar{S}_{x2}$ must be turned OFF, which can prevent shoot through within the inverter circuit [9]. The power flow paths among the primary source, secondary source, and motor are determined by the switching states of S_{x1}, S_{x2}. As shown in Fig. 3, there are three different current paths corresponding to three different switching states. When S_{x1} and S_{x2} turn ON, $\bar{S}_{x1}$ and $\bar{S}_{x2}$ turn OFF, the power that drives the motor is supplied by the primary source and the inverter phase output voltage is v_H. When $\bar{S}_{x1}$ and S_{x2} turn ON, S_{x1} and $\bar{S}_{x2}$ turn OFF, the power that drives the motor is supplied by the secondary source and the inverter phase output voltage is v_L. When $\bar{S}_{x1}$ and $\bar{S}_{x2}$ turn ON, S_{x1} and S_{x2} turn OFF, no power is supplied by the sources and the inverter phase output voltage is 0. Their corresponding three switching states in each phase are defined as $S_x \in \{0, 1, 2\}$. The gating signals, output voltages, switching states, and power source that supplies the motor are listed in Table I.

As shown, the switching state not only determines the output voltage but also the power source that supplies the motor.

B. *Decomposition of MSI*

The space vector diagram of the MSI is unsymmetrical because the dc port voltages are variable with the SoC of the energy sources. The desired voltage vector synthesis or power distribution control in this unsymmetrical SVD leads to many triangle function calculations. To reduce the computational burden, a three-level converter has conversed into a two-level one through the coordinate transformation in [32] and [33]. Based on the vector-shifted method, the three-level NPC can be simplified as a two-level converter in [34]. However, these existing methods are only based on the mathematical transformation in SVD [32], [33], [34]. On the contrary, this scheme shows clearly physical meaning. This article decomposes the MSI into subinverters I and II to avoid this complicated computation process. The idea is illustrated in Fig. 4. Subinverter I comprises two complementary active switches $S_{x1}, \bar{S}_{x1}$ in each phase and its dc-link voltage equals $v_H - v_L$. On the other hand, subinverter II comprises two complementary active switches $S_{x2}, \bar{S}_{x2}$ in each phase and its dc-link voltage equals v_L.

With the circuitry decomposition, the unsymmetrical space vector diagram of the MSI can be decomposed into subspace-vector diagram I and II, shown in Fig. 4(b). In this way, complicated sector identification and vector synthesis calculation under the unsymmetrical space vector diagram are avoided. Thus, the

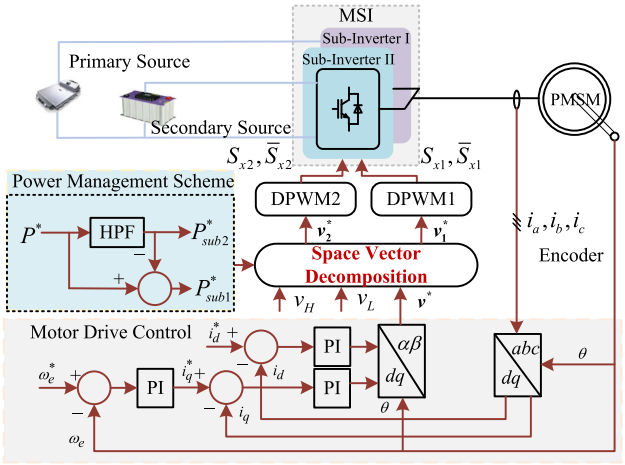

Fig. 5. Overall control diagram of the MSI.

computation burden of the modulation design for the MSI is reduced significantly.

Although the merits of space vector diagram decomposition are presented above, the constraints of switching state in each subinverter should not only meet the constraint of preventing shoot-through within the inverter circuit but also guarantee the satisfactory performance of the MSI in the subspace-vector diagram. These constraints can be summarized as follows:

1) First constraint: some switching states are not allowed in this inverter. Namely, the gating signals of (S_{x1}, S_{x2}) are not allowed to be equal to (1,0) because the current path is uncontrollable at this switching state;
2) Second constraint: the switching time of MSI in each control period should not be increased considering the system efficiency, i.e., the total switching times should not be higher than 3.

III. D^{2}PWM-Based Power Distribution Control

The overall control scheme of the D^{2}PWM-based power distribution scheme for the MSI is depicted in Fig. 5. It comprises four parts: motor drive control managed by classical field-oriented control, power flow control achieved by instantaneous power theory under the decomposed vector space frame, power management for each source regulated by a frequency splitter, and dwell time calculation for the sub inverters. Detailed descriptions of each part are given in the following text.

A. Motor Drive Control

As for the motor control, an outer speed loop is adopted to guarantee the speed reference tracking and generate i_q^*. The field-oriented control is adopted for PMSM current control. The control algorithm is implemented on the synchronous reference frame. The output of the motor controller is the voltage vector reference $\boldsymbol{v}^*$. As long as the voltage-second value for the active voltage vector remains unchanged, the motor drive control is achieved, which means the sum of the output voltage vectors of subinverter I and II equal $\boldsymbol{v}^*$

$$\boldsymbol{v}^* = \boldsymbol{v_1^*} + \boldsymbol{v_2^*} \tag{1}$$

where $\boldsymbol{v_1^*}, \boldsymbol{v_2^*}$ are the desired voltage vector for subinverters I and II, respectively.

B. Power Distribution Control With D^{2}PWM

In this article, discontinuous PWM (DPWM), which is well-known for its merits of reduced switching times and high efficiency [35], [36], [37], is employed to generate the pulse train for each subinverter. The PWM design for the subinverters is not independent because it must meet the two constraints mentioned in Section II. To meet the first constraint that the duty cycle of subinverter I is always smaller than that of subinverter II in each phase, the zero voltage vector for desired voltage vector synthesis of subinverter I is $\boldsymbol{V_0}$ (000) while the zero voltage vector for desired voltage vector synthesis of subinverter II is $\boldsymbol{V_7}$ (111).

In each control period, the current vectors of subinverters I and II are the same because subinverters share the ac ports. The output power of each subinverter can be calculated as

$$P_{\text{sub1}} = \frac{3}{2}\text{Re}\left(\bar{\boldsymbol{i}}\boldsymbol{v_1^*}\right) \tag{2}$$

$$P_{\text{sub2}} = \frac{3}{2}\text{Re}\left(\bar{\boldsymbol{i}}\boldsymbol{v_2^*}\right) \tag{3}$$

where $\bar{\boldsymbol{i}}$ denotes the conjugate of current vector $\boldsymbol{i}$.

Then, the modulation scheme design for an MSI is translated into the modulation scheme design of $\boldsymbol{v_1^*}$ and $\boldsymbol{v_2^*}$ while meeting the two constraints. Voltage vector synthesis in Sector I is employed as an example to clarify the proposed D^{2}PWM scheme and the expression for voltage vector synthesis in Sector I can be denoted as

$$\boldsymbol{v}^* = \frac{\boldsymbol{V_1}t_1 + \boldsymbol{V_2}t_2}{T_s} \tag{4}$$

where $\boldsymbol{V_1}$ (100) and $\boldsymbol{V_2}$ (110) are the basic voltage vectors, which indicates the voltage amplitudes are $\frac{2v_H}{3}$. t_1 and t_2 are the duration time for $\boldsymbol{V_1}$ and $\boldsymbol{V_2}$, respectively, and T_s is the sampling period.

To reduce the switching times and improve the efficiency of the MSI, the switching times should not be higher than 3, which means the switching times of one subinverter should not be higher than 1, and those of the other subinverter should not be higher than 2. It should be noted that the switching times of the DPWM are equal to 1 when the desired voltage vector is aligned with the basic voltage vectors and are equal to 2 in the rest conditions. Namely, one of the desired voltage vector syntheses for subinverters has to be aligned with the basic voltage vectors to meet the constraint. Based on the desired voltage vector decomposition for each subinverter, the scenarios can be categorized into two cases. Illustrations of the two cases are clarified below.

1) Desired Vector Decomposition Case I: In vector decomposition case I, the switching times of subinverter I are 2, and that of subinverter II is 1. The switching time of subinverter II is 1, indicating the desired voltage vector of subinverter II has to be aligned with one of the six basic vectors.

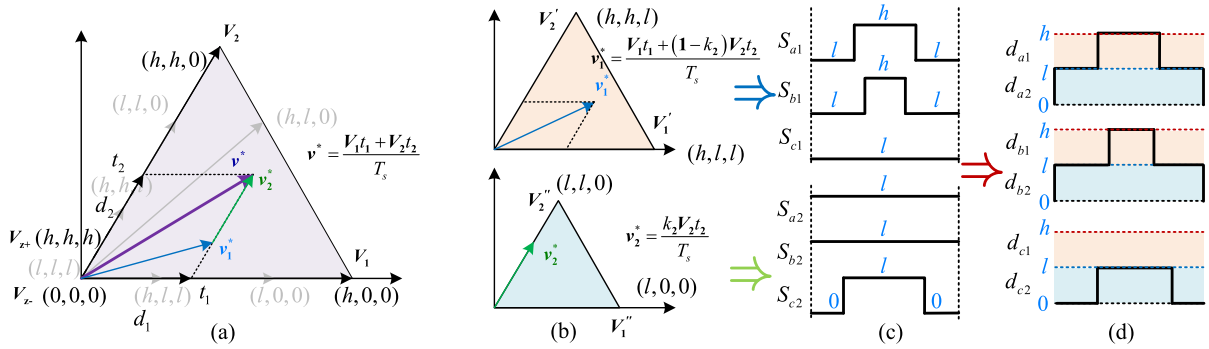

Fig. 6. Vector decomposition case I. (a) Desired voltage vector for the MSI. (b) Voltage vector decomposition in two subspace-vector diagrams. (c) DPWM in each subspace-vector diagram. (d) Synthesized pulse train for the MSI.

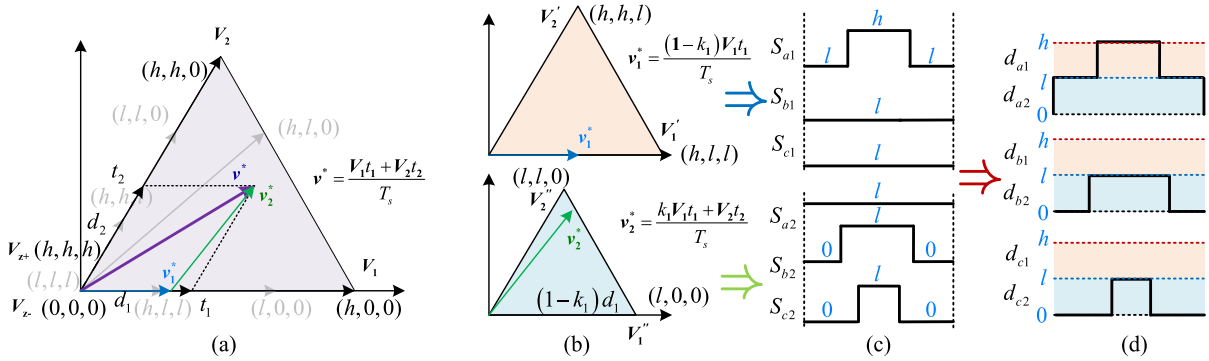

Fig. 7. Vector decomposition case II. (a) Desired voltage vector for the MSI. (b) Voltage vector decomposition in two subspace-vector diagrams. (c) DPWM in each subspace-vector diagram. (d) Synthesized pulse train for the MSI.

Besides, regarding the employment of zero voltage vector (111) to meet the first constraint for subinverter II, the basic vectors for the desired vector synthesis of subinverter II are only (110) in Sector I. On the other hand, the phase and amplitude of the desired voltage vector in subinverter I is arbitrary, which provides degrees of freedom to meet (1). The implementation process of the proposed D^{2}PWM in case I is presented in Fig. 6.

Considering the desired voltage vector of subinverter II $\boldsymbol{v_2^*}$ is aligned with $\boldsymbol{V_2}$ (110), the desired voltage vectors $\boldsymbol{v_1^*}$ and $\boldsymbol{v_2^*}$ can be represented as

$$\boldsymbol{v_1^*} = \frac{\boldsymbol{V_1}t_1 + (1-k_2)\boldsymbol{V_2}t_2}{T_s} \tag{5}$$

$$\boldsymbol{v_2^*} = \frac{k_2\boldsymbol{V_2}t_2}{T_s} \tag{6}$$

where $k_2 \in [0, 1]$ is the proportional factor available to adjust the power distribution between dc ports. The desired voltage vector decomposition process is presented in Fig. 6(a) and (b). It can also be noted that the switching time for subinverter II is only 1, and that of subinverter I is 2, as shown in Fig. 6(c). Hence, the total switching time for the MSI of the proposed D^{2}PWM is 3, whose pulse train is shown as shown in Fig. 6(d). As $\boldsymbol{v_2^*}$ is aligned with the basic vector $\boldsymbol{V_2}$ with fixed phase, the power distribution range of subinverter II is limited, and the detailed analysis is given in Section III-E.

2) Desired Vector Decomposition Case II: In vector decomposition case II, the switching times of subinverter I are 1, and that of subinverter II is 2. In this case, the switching time of subinverter I is 1, indicating the desired voltage vector of subinverter I has to be aligned with one of the six basic voltage vectors. Besides, regarding the employment of zero voltage vector (000) to meet the first constraint for subinverter I, the basic voltage vectors for desired voltage vector synthesis in subinverter I are only (001) in Sector I. The implementation process of the proposed D^{2}PWM in case II is presented in Fig. 7.

Considering the desired voltage vector of subinverter I $\boldsymbol{v_1^*}$ is aligned with $\boldsymbol{V_1}$ (100), the desired voltage vectors $\boldsymbol{v_1^*}$ and $\boldsymbol{v_2^*}$ can be represented as

$$\boldsymbol{v_1^*} = \frac{(1-k_1)\boldsymbol{V_1}t_1}{T_s} \tag{7}$$

$$\boldsymbol{v_2^*} = \frac{k_1\boldsymbol{V_1}t_1 + \boldsymbol{V_2}t_2}{T_s} \tag{8}$$

where $k_1 \in [0, 1]$ is the proportional factor available to adjust the power distribution between dc ports. The desired voltage vector decomposition process is presented in Fig. 7(a) and (b). It can also be noted that the switching time for subinverter II is only 2, and that of subinverter I is 1, as shown in Fig. 7(c). Hence, the total switching time for the MSI of the proposed D^{2}PWM is 3, whose pulse train is shown in Fig. 7(d). As $\boldsymbol{v_1^*}$ is aligned with the basic vector $\boldsymbol{V_1}$ with fixed phase, the power distribution range

of subinverter I is limited, and the detailed analysis is also given in Section III-E.

It should be noted that there is only one coefficient in each case, and this coefficient can be solved to meet the desired power distribution control. Therefore, the power distribution of the MSI with the proposed D^{2}PWM is realized by regulating the coefficients k_1, k_2.

C. Power Distribution Control Scheme

To fully explore the potential of the different energy sources, the power management scheme is inevitable in HEVs [38], [39], [40]. In this article, a simple frequency splitter is employed for power management, where the load power demand is split into low- and high-frequency components. The load demand frequency decoupling is achieved through a high-pass filter [41]. The high-frequency component is fed into the fast-acting power sources (secondary source in this paper), noted as P_s^*, such as the supercapacitor, and the rest of the components are fed into the slow-acting sources (primary source in this article), noted as P_p^*, such as fuel cells and batteries. To realize the power management scheme, the power distribution control of the MSI is mandatory. The power distribution control is achieved by regulating the coefficients k_1, k_2.

Combining (3), (6), the output power of subinverter II can be rewritten as

$$P_{\text{sub2}} = \frac{3}{2}\text{Re}\left(\bar{\boldsymbol{i}}\frac{k_2\boldsymbol{V_2}t_2}{T_s}\right) \tag{9}$$

The output power of subinverter II is exactly the output power of the low-voltage port. By setting the output power of the secondary source to the subinverter II, namely, $P_s^* = P_{\text{sub2}}$, the coefficient k_2 can be obtained. If the obtained k_2 is within [0,1], then the desired voltage vectors $\boldsymbol{v_1^*}$ and $\boldsymbol{v_2^*}$ for subinverter I and II can be calculated.

Otherwise, the feasible solution for the power distribution control is in vector decomposition case II. In this case, k_2 is set to 0. Equations (3) and (8) are combined to calculate the value of k_1. The resulting equation can be rewritten as

$$P_{\text{sub2}} = \frac{3}{2}\text{Re}\left(\bar{\boldsymbol{i}}\frac{k_1\boldsymbol{V_1}t_1 + \boldsymbol{V_2}t_2}{T_s}\right). \tag{10}$$

If k_1 is within [0,1], the desired voltage vectors $\boldsymbol{v_1^*}$ and $\boldsymbol{v_2^*}$ for subinverters I and II can be obtained. Otherwise, no feasible solution is available for the power distribution control, which indicates the desired power distribution range is beyond the power distribution capability of the MSI. In this case, k_1 and k_2 are set to 0 to protect the MSI.

D. Dwell Time Calculation of the Subinverters

In the last step, the desired voltage vectors $\boldsymbol{v_1^*}$ and $\boldsymbol{v_2^*}$ for subinverters are obtained by solving k_1 and k_2. The dwell time calculation in Sector I is illustrated as an example to show the implementation process of the dwell time calculation in subinverters.

The dwell time of subinverter I can be obtained by

$$t_1' = \frac{(1-k_1)\boldsymbol{V_1}t_1}{\boldsymbol{V_1'}} = \frac{(1-k_1)t_1}{1-\xi} \tag{11}$$

$$t_2' = \frac{(1-k_2)\boldsymbol{V_2}t_2}{\boldsymbol{V_2'}} = \frac{(1-k_2)t_2}{1-\xi} \tag{12}$$

where $\boldsymbol{V_1'}$ and $\boldsymbol{V_2'}$ are the basic voltage vectors for subinverter I in Sector I. t_1' and t_2' are the dwell time of $\boldsymbol{V_1'}$ and $\boldsymbol{V_2'}$, respectively. $\xi = \frac{v_L}{v_H}$ is the voltage ratio of the sources.

The dwell time of subinverter II can be obtained by

$$t_1'' = \frac{k_1\boldsymbol{V_1}t_1}{\boldsymbol{V_1''}} = \frac{k_1 t_1}{\xi} \tag{13}$$

$$t_2'' = \frac{k_2\boldsymbol{V_2}t_2}{\boldsymbol{V_2''}} = \frac{k_2 t_2}{\xi} \tag{14}$$

where $\boldsymbol{V_1''}$ and $\boldsymbol{V_2''}$ are the basic voltage vectors for subinverter II in Sector I. t_1'' and t_2'' are the dwell time of $\boldsymbol{V_1''}$ and $\boldsymbol{V_2''}$, respectively.

The gating signals of (S_{x1}, S_{x2}) are not allowed to be equal to (1,0) in the MSI because the current path is not controllable at this switching state. To meet this constraint, the zero vector for voltage vector synthesis in subinverter I is $\boldsymbol{V_0}(000)$, and that in subinverter II is $\boldsymbol{V_7}(111)$.

Taking Sector I as an example, the desired voltage vectors of $\boldsymbol{v_1^*}$ and $\boldsymbol{v_2^*}$ are synthesized by active voltage vector $\boldsymbol{V_1}(100)$, $\boldsymbol{V_2}(110)$. The dwell time for inverter I can be calculated as

$$\begin{cases} t_{a1} = t_1' + t_2' \\ t_{b1} = t_2' \\ t_{c1} = 0 \end{cases} \tag{15}$$

where $t_{x1} \in [0, T_s], x \in \{a, b, c\}$.

The duration time for inverter II can be calculated as

$$\begin{cases} t_{a2} = t_1'' + t_2'' + t_0'' \\ t_{b2} = t_2'' + t_0'' \\ t_{c2} = t_0'' \end{cases} \tag{16}$$

where $t_0'' = T_s - t_1'' - t_2'' > 0$. $d_{x2} \in [0, T_s], x \in \{a, b, c\}$. According to (15) and (16), it is obvious that $d_{a2} \geq d_{a1}, d_{b2} \geq d_{b1}$, and $d_{c2} \geq d_{c1}$. The constraint is satisfied.

E. Power Distribution Range Analysis

With the proposed D^{2}PWM scheme, the MSI can regulate the output power between the dc source. Combined with (2) and (3), the output power of each port is determined by the load current $\boldsymbol{i}$ and the output vector of each port. The power distribution range η, defined as the power of secondary source P_{sub2} divided by the total output power P, can be expressed as

$$\eta = \frac{P_{\text{sub2}}}{P} = \xi\frac{|\boldsymbol{v_2^*}|}{|\boldsymbol{v^*}|}. \tag{17}$$

According to (1), the synthesis of $\boldsymbol{v^*}$ can be expressed in scalar form as

$$\boldsymbol{v^*} = |\boldsymbol{v_1^*}||\boldsymbol{v_2^*}|\cos\theta \tag{18}$$

where θ is the angle between $\boldsymbol{v_1^*}$ and $\boldsymbol{v_2^*}$, and $0^o \leq \theta \leq 60^o$ in sector I. If the motor only operates in the liner modulation range,

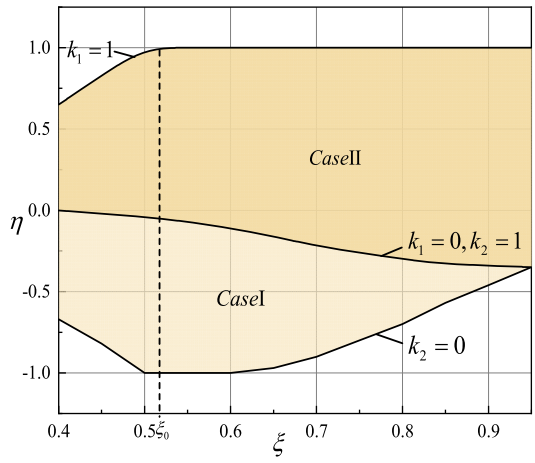

Fig. 8. Curve of the power regulation ratio at rated torque and speed.

the ranges of $\boldsymbol{v_1^*}$, $\boldsymbol{v_2^*}$ and $\boldsymbol{v^*}$ can be calculated as

$$0 \le |\boldsymbol{v_1^*}| \le \frac{v_H - v_L}{\sqrt{3}} \tag{19}$$

$$0 \le |\boldsymbol{v_2^*}| \le \frac{v_L}{\sqrt{3}} \tag{20}$$

$$0 \le |\boldsymbol{v^*}| \le \frac{v_H}{\sqrt{3}}. \tag{21}$$

In case I, when $\boldsymbol{v_2^*}$ is aligned with the basic voltage vector $\boldsymbol{V_2}$, $|\boldsymbol{v_2^*}|$ reaches the maximum value $\frac{v_L}{\sqrt{3}}$, and $0^0 \le \theta \le 60^0$. So the power distribution range η can be written as

$$\frac{\sqrt{3}\xi|\boldsymbol{v^*}|}{v_L} \le \eta \le \frac{2\sqrt{3}\xi|\boldsymbol{v^*}|}{v_L}. \tag{22}$$

Similarly, when the synthesized voltage vector decomposition corresponds to case II, $\boldsymbol{v_1^*}$ of the subinverter I is aligned with the basic voltage vector $\boldsymbol{V_1}$, $|\boldsymbol{v_1^*}|$ reaches the maximum value $\frac{v_H - v_L}{\sqrt{3}}$, and the power distribution range η can be calculated as

$$\frac{\sqrt{3}\xi|\boldsymbol{v^*}|}{v_H - v_L} \le \eta \le \frac{2\sqrt{3}\xi|\boldsymbol{v^*}|}{v_H - v_L}. \tag{23}$$

Combining (22) and (23), the theoretical power distribution range can be calculated as

$$\left\{\frac{\sqrt{3}\xi|\boldsymbol{v^*}|}{v_L}, \frac{\sqrt{3}\xi|\boldsymbol{v^*}|}{v_H - v_L}\right\}_{\min} \le \eta \le \left\{\frac{2\sqrt{3}\xi|\boldsymbol{v^*}|}{v_L}, \frac{2\sqrt{3}\xi|\boldsymbol{v^*}|}{v_H - v_L}\right\}_{\max} \tag{24}$$

where $|\boldsymbol{v^*}|$ is determined by the modulation index, while ξ is determined by the voltage ratios. Based on the above analysis, it can be inferred that the power distribution range can reach the maximum value when the voltage ratio $0.52 \le \xi \le 0.61$ under the rated working conditions. The power distribution range is given, and the relationship between η and k is illustrated in Fig. 8.

IV. Experimental Results

The experimental test rig of the MSI-fed PMSM drive was built in the laboratory to verify the effectiveness of the proposed

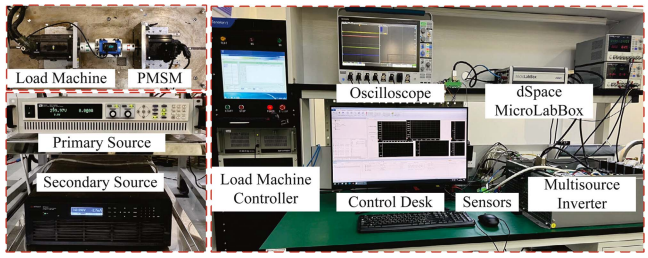

Fig. 9. Experimental test rig.

TABLE II
System Parameters

Parameters	value	Parameters	value
Primary Source Voltage	300 V	Secondary Source Voltage	125−175 V
Rated Power	1 kW	Rated Torque	8 Nm
Rated Speed	1000 r/min	Rated Current (RMS)	5 A
Rotor Flux	0.41 Wb	Pole Pairs	4
Stator Inductance	3.54 mH	Stator Resistance	1.25 Ω
Sampling Period	50 μs	Dead Time	1.5 μs
DC-link capacitor	5000 μF		

D^{2}PWM, as shown in Fig. 9, whose detailed experimental parameters are listed in Table II. In this article, the voltage of the primary source is set to 300 V, and the voltage of the secondary source is set to 125–175 V to emulate the source voltage variations in practical applications. Two programmable dc sources are employed as the hybrid energy sources, where the primary source emulates a slow-acting source, and the secondary source emulates a fast-acting source. A dSPACE MicroLabBox DS1202 was adopted to implement the digital control, and a slave Xilinx was applied to generate the gate signals for each switch. A 5000 pulse incremental encoder is equipped to obtain the rotor speed and position. A commercial software-driven induction motor, which was connected to the PMSM, was utilized as a load machine. The load machine can operate in the torque mode to generate the desired load torque.

A. Steady-State Performance

In the following, the steady-state performance of the MSI with the proposed scheme is investigated.

1) Results Under Variable Port Voltage: Considering the dc source voltage variations in practical applications, the proposed scheme under different voltage ratios is tested first. Fig. 10 presents the steady-state performance to verify the effectiveness of the proposed D^{2}PWM scheme at different voltage ratios, where V_H is set to 300 V and V_L is set to 125, 150, and 175 V, respectively. The experimental results are conducted at rated torque and rated speed. It is seen that the proposed scheme presents satisfactory control performance under different voltage ratios. As shown, the sinusoidal waveform of the stator current can be observed in all scenarios. Although the input voltages are unbalanced, the tracking of d- and q-axes current reference is not affected, indicating the proposed scheme is effective under variable dc-link voltage.

2) Results Under Different Power Flow Modes: To verify the effectiveness of D^{2}PWM in power distribution and the capability

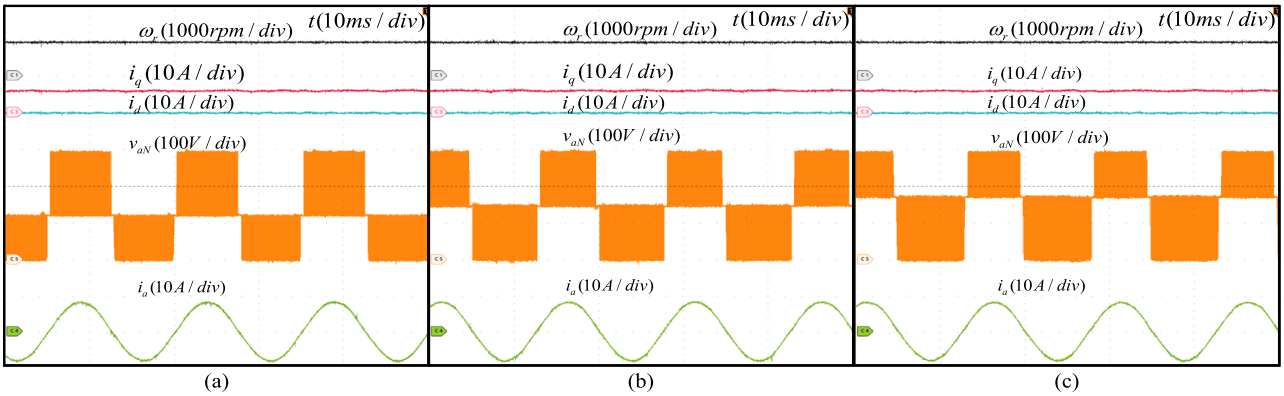

Fig. 10. Steady-state performance of unbalanced dc links at the rated speed with the rated load torque. (a) $v_H = 300$ V, $v_L = 125$ V. (b) $v_H = 300$ V, $v_L = 150$ V. (c) $v_H = 300$ V, $v_L = 175$ V. From top to bottom, the waveform is rotor speed ω_r, q-axis current i_q, d-axis current i_d, phase a voltage v_{aN} and phase a current i_a, respectively.

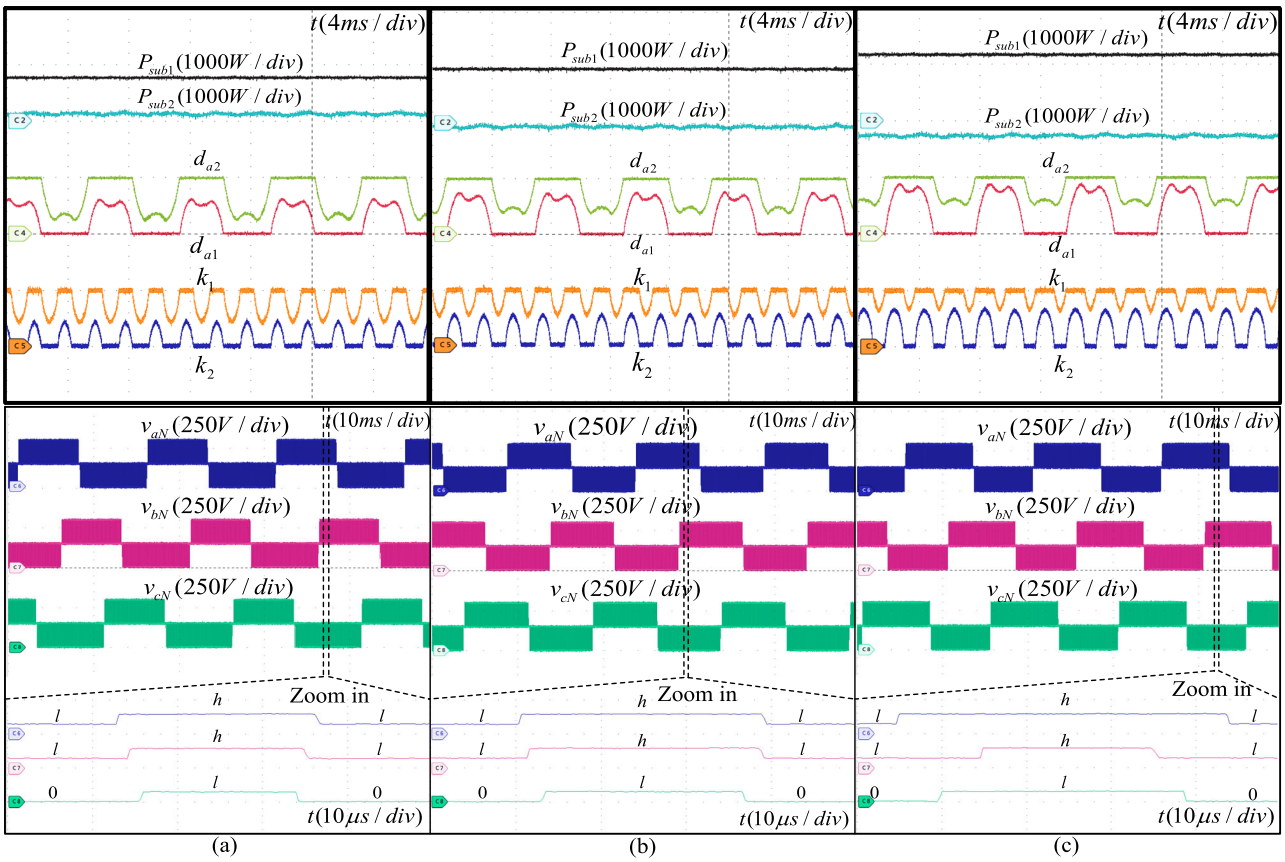

Fig. 11. Steady-state performance of three power flow modes with the rated speed and rated load torque. (a) $P^*_{\text{sub1}} = 800$ W. (b) $P^*_{\text{sub1}} = 1000$ W. (c) $P^*_{\text{sub1}} = 1200$ W. From top to bottom, the waveform is output power of primary and secondary sources P_{sub1} and P_{sub2}, the modulation signals d_{a1} and d_{a2}, power coefficients k_1 and k_2, phase voltage v_{aN}, v_{bN}, v_{cN}, respectively.

of total switching times being 3, Fig. 11 shows the proposed strategy under different power flow modes with the switching status of every phase. As shown in Fig. 11(a), 800 W is supplied by the primary source while the secondary source supplies the secondary one. The desired power P^* is set to 1000 W, and the motor operates the rated speed and rated load torque to verify the performance in scenario 1. As shown in Fig. 11(b), the primary source supplies all the power, P^* is set to 1000 W, and the motor operates the rated speed and rated load torque to verify the performance in scenario 2. The primary source solely supplies the desired power. As shown in Fig. 11(c), 1200 W is supplied by the primary source while the secondary source absorbs 200 W power. The motor can operate in different modes by setting P^*_{sub1}. In scenarios 1-3, the MSI operates in the seven-segment pulsewidth modulation. It can be observed that the MSI has been decoupled into two two-level inverters successfully from the

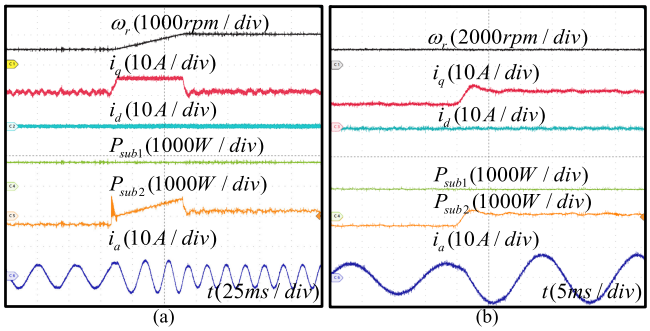

Fig. 12. (a) Dynamic performance of speed change from 500 to 1000 r/min at rated torque. (b) Dynamic performance of load torque step change from 5 to 8 N · m at rated speed. From top to bottom, the waveform is speed, d- and q-axes current, the output power of the primary and secondary source, and phase a current.

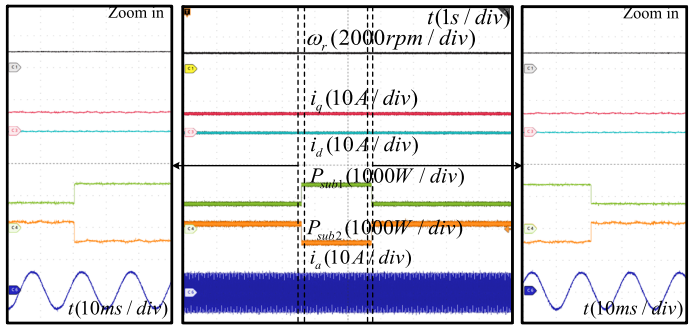

Fig. 13. Dynamic performance of port power distribution stepped change with P^* reference stepped from 800 to 1400 W then stepped back to 800 W. From top to bottom, the waveform is speed, d- and q- axes current, the output power of primary and secondary sources, and phase a current.

modulation signal d_{a1} and d_{a2}. Moreover, it can be concluded that both subinverters employ the DPWM strategy by observing the coefficient k_1 and k_2, and the total number of switching times is reduced to 3 with the switching status in a control period.

As the power management scheme decouples the power demand into high- and low-frequency components, the power reference for the primary source is set to constant. As shown in the above three scenarios, the instantaneous output power of the primary source operates at a constant value, while the secondary source tracks the high-frequency component of the power demand.

B. Dynamic Performance

Apart from the steady-state performance, the dynamic performance is also investigated to show the effectiveness of the proposed scheme. The dynamic response of the stepped change in the speed reference and load torque is illustrated in Fig. 12, respectively. Fig. 12(a) presents the performance of the stepped change in the speed reference response from half to the full rated speed of 1000 r/min. It is seen that the motor presents fast speed dynamics with maximum torque acceleration. During the process, the output power of the primary source is controlled at 800 W, and the output power of the secondary source varies with the speed-changing process. The dynamic response of the stepped change in the load torque with the proposed method is presented in Fig. 12(b). In the test, the rotor runs at the rated speed of 1000 r/min, and then, an external load torque is stepped change using a load machine from 5 to 8 N · m. During the step change of operation point, the system remains stable with i_d and i_q, and machine speed is well regulated while the output power of the slow-active source remains unchanged and that of the fast-acting source varies with the operating point changing, indicating the effectiveness of the proposed power distribution scheme for energy management during the speed/torque variation process.

Besides, the step change of source output power is also investigated to show the dynamic performance in power distribution control. The dynamic response of stepped change in the primary source output power reference with the proposed scheme is presented in Fig. 13. In the test, the motor runs at rated speed and rated torque, and the reference power of the primary source is first set to 800 W, then changed to 1400 W, and finally stepped back to 800 W. From the zoomed-in figure, it should be noted that the output power of the primary source changes very fast in the control period, and the motor drive control is not affected during the source output power stepped change process, indicating the fast power distribution control can be achieved by the proposed D^{2}PWM scheme.

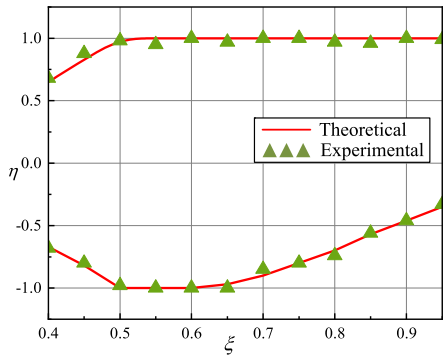

Fig. 14. Curve of the experiment verification about the power distribution range η under different voltage ratios ξ.

C. Power Distribution Range Verification

The power distribution capability of the MSI under different voltage ratios ξ was also experimentally tested in Fig. 14. As shown in Fig. 14, it can be concluded that the experimental curve matches the theoretical curve well. When the voltage ratio ξ varies from 0.40 to 0.95, the power distribution capability is from -1.03 to 1.00. With the increase of the voltage ratio ξ, the power distribution range of the MSI first expands to the maximum range and then decreases. When ξ reaches 0.53, the maximum value of η equals 1, meaning the secondary source can provide the load power without using the primary source. To obtain a larger power distribution range for the MSI, the voltage ratio ξ should be set to an appropriate value. The experimental results, which are consistent with the theoretical results, verify the analysis in Section III.

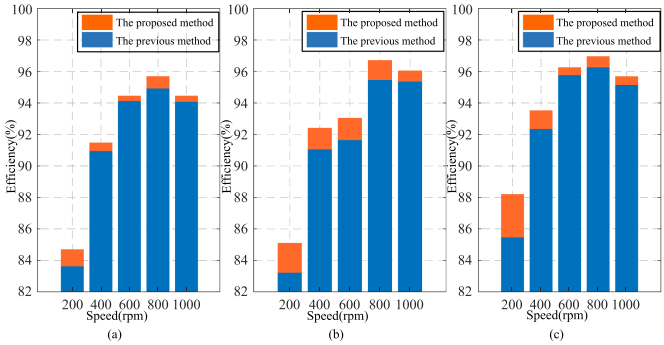

Fig. 15. Efficiency comparison of the proposed D^{2}PWM scheme and the conventional linear vector space decomposition method [30] under different voltage ratios at full speed range with rated load. (a) $\xi = 0.4$. (b) $\xi = 0.5$. (c) $\xi = 0.6$.

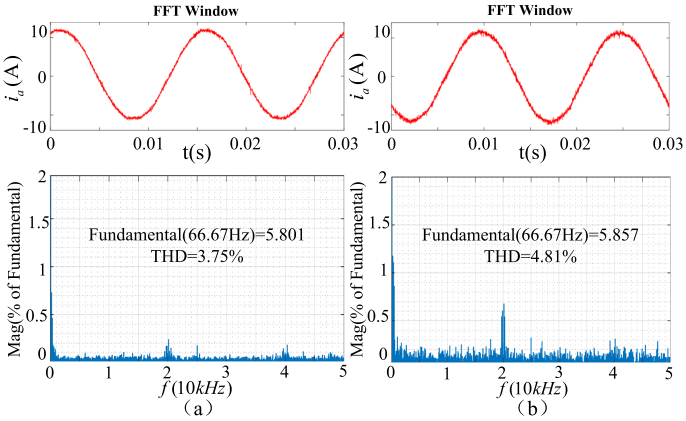

Fig. 16. Current FFT results. (a) The proposed method. (b) The previous method [30]. From top to bottom, the waveform is the phase a current and its spectrum.

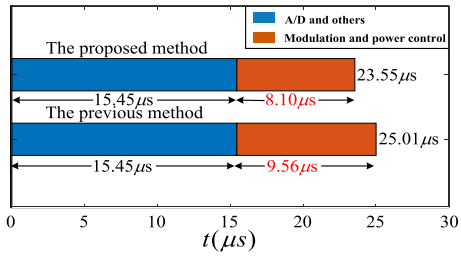

Fig. 17. Tested execution time of the proposed method and the previous method [30].

D. Comparison With the Existing Scheme

The comparative study between the proposed method and the previous methods [30] in terms of the power conversion efficiency, THD of the current, and computational burden are presented in this part.

1) Power Conversion Efficiency: The power conversion efficiency of the proposed method and the previous method [30] under different voltage ratios is tested using YOKOGWA WT1803E Precision Power Analyzer, and presented in Fig. 15. As shown, the proposed scheme demonstrates an improvement in power conversion efficiency even when the port voltage is unbalanced. Besides, when the port voltage is balanced, the proposed method shows a more significant improvement compared to the unbalanced state at full speed range with rated load. On the other hand, the efficiency curves are tested at different speeds, varying from 200 to 1000 r/min. Due to the reduction of switching losses, the power conversion efficiency of the MSI has increased by an average of 1.17%. When the speed is below the rated operating conditions, the improvement in power conversion efficiency is more significant, reaching a maximum of 1.89% and a minimum of 0.59% at the rated speed. Therefore, the D^{2}PWM strategy has a greater advantage in terms of power conversion efficiency compared to the previous method [30].

2) THD of the Current: The current FFT analysis of the proposed method and the previous method [30] is tested, and the harmonics spectrum is presented in Fig. 16. The data are acquired from an oscilloscope at 1 MHz sampling frequency and analyzed in MATLAB. As shown, the current THD of the previous method [30] and the proposed method is 4.81% and 3.75%, respectively. Therefore, it is evident that the D^{2}PWM scheme can improve the quality of the output current.

3) Computational Burden: The execution time of the proposed method and the previous one [30] is tested using dSpace profiler 3.8, and presented in Fig. 17. As shown, it costs 15.45 μs to implement A/D and other calculation processes in the hardware layer, 9.56 μs to implement algorithms of the modulation and power control in [30] while 8.10 μs to implement algorithms of the modulation and power control in the proposed method. Based on these results, it can be obtained that the 15.3% computational burden reduction (except the calculation of A/D and others) is achieved by the proposed method in comparison with the previous one [30], which indicates that the proposed method has a higher computing efficiency with the decoupled power distribution model.

TABLE III
COMPARISON WITH THE EXISTING SCHEMES

Schemes	Power Conversion Efficiency	Computational Burden	Electricity Quality
[42]	Low	Large	Good
[43]	Low	Medium	Good
[26]	Medium	Large	Medium
[11]	Low	Medium	Good
[29]	High	Large	Medium
[15]	Medium	Medium	Good
[30]	Medium	Medium	Good
Proposed	High	Small	Good

4) Theoretical Comparisons: As shown in Table III, we compared the existing methods of power distribution strategy on power conversion efficiency, computational burden, and electricity quality. In [11], [26], [42], [43], the flexible power distribution is achieved by introducing extra dc–dc converters and PI loops, which leads to lower power conversion efficiency and a heavy computational burden. On the other hand, the power distribution strategies [15], [29], [30] are designed without the help of dc–dc converter. In [29], an outer control loop and inner modulation strategy are applied to achieve high power conversion efficiency, but it is not worth the cost of computational burden and electricity quality. Although the computational burden and electricity quality are reduced in [15] and [30], these methods present

medium power conversion efficiency due to the high switching losses in nine-segment pulsewidth modulation. By contrast, the proposed D^{2}PWM-based power distribution control scheme can realize flexible power distribution without employing dc–dc converters, presenting high-efficiency features with total switching times of 3. Besides, the computational burden of the proposed method can also be reduced with direct power distribution modeling and decoupled modulation processes without affecting motor drive control.

V. Conclusion

To simplify the modulation design and reduce the switching losses of the MSI, this article proposes a D^{2}PWM-based power distribution control scheme, where the MSI is decomposed into two-level subinverters to avoid the heavy computational burden in the unsymmetrical space-vector diagram. A D^{2}PWM scheme, which guarantees the total switching times of 3, is further analyzed and developed to reduce the switching losses. An intuitive decoupled power flow control for each port without affecting the motor drive control can be easily developed with the proposed D^{2}PWM model. Experiments were conducted to verify the effectiveness of the proposed scheme. Compared with that of the linear vector space decomposition method [30], the advantages of the proposed D^{2}PWM scheme can be concluded as:

1) The power conversion efficiency of the proposed scheme is improved by around 1.17%.
2) The THD of the output current is improved by 1.06%.
3) The computational burden is reduced by 15.27%.

However, it should be noted that there is no extra control freedom degree in the proposed method to suppress the common mode voltage of the motor, and it remains to be future work.

References

[1] B. K. Bose, "Global energy scenario and impact of power electronics in 21st century," *IEEE Trans. Ind. Electron.*, vol. 60, no. 7, pp. 2638–2651, Jul. 2013.

[2] A. Biswas and A. Emadi, "Energy management systems for electrified powertrains: State-of-the-art review and future trends," *IEEE Trans. Veh. Technol.*, vol. 68, no. 7, pp. 6453–6467, Jul. 2019.

[3] M. Ehsani, K. V. Singh, H. O. Bansal, and R. T. Mehrjardi, "State of the art and trends in electric and hybrid electric vehicles," *Proc. IEEE*, vol. 109, no. 6, pp. 967–984, Jun. 2021.

[4] J. Reimers, L. Dorn-Gomba, C. Mak, and A. Emadi, "Automotive traction inverters: Current status and future trends," *IEEE Trans. Veh. Technol.*, vol. 68, no. 4, pp. 3337–3350, Apr. 2019.

[5] S. J. Rind, Y. Ren, Y. Hu, J. Wang, and L. Jiang, "Configurations and control of traction motors for electric vehicles: A review," *Chin. J. Elect. Eng.*, vol. 3, no. 3, pp. 1–17, 2017.

[6] E. Fedele, A. Cervone, I. Spina, D. Iannuzzi, and A. D. Pizzo, "Multiobjective vector modulation for improved control of NPC-based multi-source inverters in hybrid traction systems," *IEEE J. Emerg. Sel. Top. Power Electron.*, vol. 10, no. 6, pp. 7464–7474, Dec. 2022.

[7] L. Dorn-Gomba, P. Magne, B. Danen, and A. Emadi, "On the concept of the multi-source inverter for hybrid electric vehicle powertrains," *IEEE Trans. Power Electron.*, vol. 33, no. 9, pp. 7376–7386, Sep. 2018.

[8] O. Salari, K. H. Zaad, A. Bakhshai, and P. Jain, "Hybrid energy storage systems for electric vehicles: Multi-source inverter topologies," in *Proc. 14th Int. Conf. Power Electron.*, 2018, pp. 111–116.

[9] Z. Huang, D. Zhou, L. Wang, Z. Shen, and Y. Li, "A review of single-stage multiport inverters for multisource applications," *IEEE Trans. Power Electron.*, vol. 38, no. 5, pp. 6566–6584, May 2023.

[10] Z. Huang, D. Zhou, Z. Shen, and J. Zou, "Directed graph-based topology derivation method for single-stage multiport inverters," *IEEE Trans. Power Electron.*, vol. 38, no. 11, pp. 14614–14627, Nov. 2023.

[11] L. Dorn-Gomba, J. Guo, and A. Emadi, "Multi-source inverter for power-split hybrid electric powertrains," *IEEE Trans. Veh. Technol.*, vol. 68, no. 7, pp. 6481–6494, Jul. 2019.

[12] E. Fedele, D. Iannuzzi, P. Tricoli, and A. D. Pizzo, "NPC-based multi-source inverters for multimode DC rail traction systems," *IEEE Trans. Transp. Electrific.*, vol. 9, no. 1, pp. 1289–1299, Mar. 2023.

[13] X. Wu, G. Tan, Z. Ye, G. Yao, Z. Liu, and G. Liu, "Virtual-space-vector PWM for a three-level neutral-point-clamped inverter with unbalanced DC-links," *IEEE Trans. Power Electron.*, vol. 33, no. 3, pp. 2630–2642, Mar. 2018.

[14] C. Yan, D. Xu, and W. Chen, "General control scheme for a dual-input three-level inverter," *IEEE Trans. Power Electron.*, vol. 34, no. 2, pp. 1838–1850, Feb. 2019.

[15] D. Zhou, K. Luo, Z. Shen, and J. Zou, "Deadbeat power distribution control of single-stage multiport inverter-fed PMSM drive for hybrid electric vehicles," *IEEE Trans. Power Electron.*, vol. 38, no. 6, pp. 7586–7597, Jun. 2023.

[16] L. Liu, D. Zhou, J. Zou, Z. Shen, and X. Fu, "Direct duty cycle control-based power allocation strategy for single-stage multiport inverter in islanded microgrid," *IEEE Trans. Power Electron.*, vol. 38, no. 12, pp. 14956–14967, Dec. 2023.

[17] D. Zhou, L. Ding, and Y. R. Li, "Two-stage model predictive control of neutral-point-clamped inverter-fed permanent-magnet synchronous motor drives under balanced and unbalanced DC links," *IEEE Trans. Ind. Electron.*, vol. 68, no. 5, pp. 3750–3759, May 2021.

[18] L. Liu, D. Zhou, J. Zou, and W. Wang, "Zero-vector-regulation-based closed-loop power distribution strategy for dual-dc-port dc-ca converter-connected PV-battery hybrid systems," *IEEE Trans. Power Electron.*, vol. 38, no. 6, pp. 6956–6968, Jun. 2023.

[19] C. Xue, J. Wang, and Y. Li, "Model predictive control for grid-tied multi-port system with integrated pv and battery storage," *IEEE Trans. Smart Grid*, vol. 13, no. 6, pp. 4596–4609, Nov. 2022.

[20] J. Ebrahimi, O. Salari, S. Eren, K. Hashtrudi-Zaad, A. Bakhshai, and P. Jain, "Efficiency improved multi-source inverter for hybrid energy storage systems in electric vehicle application," *IEEE Trans. Power Electron.*, vol. 37, no. 2, pp. 1982–1997, Feb. 2022.

[21] D. Zhou, Z. Zhang, Z. Shen, and J. Zou, "Modulated model predictive control of multisource inverters with flexible power distribution," *IEEE Trans. Ind. Electron.*, early access, 2024, doi: 10.1109/TIE.2024.3374397.

[22] Z. Ye, Y. Xu, X. Wu, G. Tan, X. Deng, and Z. Wang, "A simplified PWM strategy for a neutral-point-clamped (NPC) three-level converter with unbalanced DC links," *IEEE Trans. Power Electron.*, vol. 31, no. 4, pp. 3227–3238, Apr. 2016.

[23] C. Qin, X. Li, X. Xing, C. Zhang, and G. Zhang, "Common-mode voltage reduction method for three-level inverter with unbalanced neutral-point voltage conditions," *IEEE Trans. Ind. Inform.*, vol. 17, no. 10, pp. 6603–6613, Oct. 2021.

[24] X. Wu, G. Tan, G. Yao, C. Sun, and G. Liu, "A hybrid PWM strategy for three-level inverter with unbalanced DC links," *IEEE J. Emerg. Sel. Topics Power Electron.*, vol. 6, no. 1, pp. 1–15, Mar. 2018.

[25] H. Wu, J. Wang, T. Liu, T. Yang, and Y. Xing, "Modified SVPWM-controlled three-port three-phase AC-DC converters with reduced power conversion stages for wide voltage range applications," *IEEE Trans. Power Electron.*, vol. 33, no. 8, pp. 6672–6686, Aug. 2018.

[26] D. Zhou, J. Wang, N. Hou, Y. Li, and J. Zou, "Dual-port inverters with internal DC-DC conversion for adjustable DC-link voltage operation of electric vehicles," *IEEE Trans. Power Electron.*, vol. 36, no. 6, pp. 6917–6928, Jun. 2021.

[27] Y. Zou et al., "Dynamic-space-vector discontinuous PWM for three-phase vienna rectifiers with unbalanced neutral-point voltage," *IEEE Trans. Power Electron.*, vol. 36, no. 8, pp. 9015–9026, Aug. 2021.

[28] Q. Yan, L. Xiao, H. Chen, X. Yuan, H. Xu, and R. Zhao, "An analytical discontinuous space-vector PWM for three-level inverters with unbalanced DC-link voltages," *IEEE Trans. Power Electron.*, vol. 37, no. 7, pp. 7718–7728, Jul. 2022.

[29] J. Wang, K. Sun, D. Zhou, and Y. Li, "Virtual SVPWM-based flexible power control for dual-DC-port dc-ac converters in PV-battery hybrid systems," *IEEE Trans. Power Electron.*, vol. 36, no. 10, pp. 11431–11443, Oct. 2021.

[30] D. Zhou, K. Luo, Z. Shen, and J. Zou, "Vector-space-decomposition-based power flow control of single-stage-multiport-inverter-fed PMSM drive for hybrid electric vehicles," *IEEE Trans. Ind. Electron.*, vol. 71, no. 8, pp. 8514–8524, Aug. 2024.
[31] L. Liu, D. Zhou, J. Zou, and W. Wang, "Decoupled modeling and wide-range power distribution strategy for the multisource inverter in microgrids," *IEEE Trans. Power Electron.*, vol. 38, no. 10, pp. 12078–12090, Oct. 2023.
[32] Z. He et al., "A hybrid DPWM for Vienna rectifiers based on the three-level to two-level conversion," *IEEE Trans. Ind. Electron.*, vol. 69, no. 9, pp. 9429–9439, Sep. 2022.
[33] Z. He et al., "A novel method to evaluate the influence of Vienna rectifier neutral-point voltage fluctuation on input current quality," *IEEE Trans. Power Electron.*, vol. 36, no. 7, pp. 8347–8358, Jul. 2021.
[34] D. Zhou, C. Jiang, Z. Quan, and Y. R. Li, "Vector shifted model predictive power control of three-level neutral-point-clamped rectifiers," *IEEE Trans. Ind. Electron.*, vol. 67, no. 9, pp. 7157–7166, Sep. 2020.
[35] S. Mukherjee, S. K. Giri, and S. Banerjee, "A flexible discontinuous modulation scheme with hybrid capacitor voltage balancing strategy for three-level NPC traction inverter," *IEEE Trans. Ind. Electron.*, vol. 66, no. 5, pp. 3333–3343, May 2019.
[36] S. Mukherjee, S. K. Giri, S. Kundu, and S. Banerjee, "A generalized discontinuous PWM scheme for three-level NPC traction inverter with minimum switching loss for electric vehicles," *IEEE Trans. Ind. Appl.*, vol. 55, no. 1, pp. 516–528, Jan./Feb. 2019.
[37] Z. Zhang, O. C. Thomsen, and M. A. E. Andersen, "Discontinuous PWM modulation strategy with circuit-level decoupling concept of three-level neutral-point-clamped (NPC) inverter," *IEEE Trans. Ind. Electron.*, vol. 60, no. 5, pp. 1897–1906, May 2013.
[38] Q. Zhang and G. Li, "Experimental study on a semi-active battery-supercapacitor hybrid energy storage system for electric vehicle application," *IEEE Trans. Power Electron.*, vol. 35, no. 1, pp. 1014–1021, Jan. 2020.
[39] Q. Xu et al., "A decentralized dynamic power sharing strategy for hybrid energy storage system in autonomous DC microgrid," *IEEE Trans. Ind. Electron.*, vol. 64, no. 7, pp. 5930–5941, Jul. 2017.
[40] X. Zhang, B. Wang, D. Gamage, and A. Ukil, "Model predictive and iterative learning control based hybrid control method for hybrid energy storage system," *IEEE Trans. Sustain. Energy*, vol. 12, no. 4, pp. 2146–2158, Oct. 2021.
[41] H. Alloui, Y. Achour, K. Marouani, and M. Becherif, "Energy management based on frequency decoupling: Experimental results with fuel cell-electric vehicle emulator," in *Proc. IEEE 81st Veh. Technol. Conf.*, 2015, pp. 1–5.
[42] Z. Yi, W. Dong, and A. H. Etemadi, "A unified control and power management scheme for PV-battery-based hybrid microgrids for both grid-connected and islanded modes," *IEEE Trans. Smart Grid.*, vol. 9, no. 6, pp. 5975–5985, Nov. 2018.
[43] A. Merabet, K. T. Ahmed, H. Ibrahim, R. Beguenane, and A. M. Y. M. Ghias, "Energy management and control system for laboratory scale microgrid based wind-PV-battery," *IEEE Trans. Sustain. Energy*, vol. 8, no. 1, pp. 145–154, Jan. 2017.

Dehong Zhou (Senior Member, IEEE) received the B.Sc. and Ph.D. degrees in control science and engineering from Huazhong University of Science and Technology, Wuhan, China, in 2012 and 2016, respectively.

He was a Postdoctoral Research Fellow with Nanyang Technological University, Singapore, and University of Alberta, Canada. Since 2020, he has been a Full Professor with the School of Automation Engineering, University of Electronic Science and Technology of China, Chengdu, China, and Shenzhen Institute for Advanced Study, UESTC, Shenzhen, China. His research interests include power electronics and motor drives.

Zhao Zhang (Student Member, IEEE) was born in Sichuan, China. He received the B.S. degree in mechanical and electrical engineering from Southwest Petroleum University, Chengdu, China, in 2022. He is currently working toward the Ph.D. degree in control science and engineering with the School of Automation Engineering, University of Electronic Science and Technology of China, Chengdu, China.

His research interests include multisource inverters and motor drives.

Xin Liu (Member, IEEE) received the B.S. degree in electrical engineering from Wuhan University, Wuhan, China, in 2015, and the Ph.D. degree in electrical engineering from Shanghai Jiao Tong University, Shanghai, China, in 2019.

From 2019 to 2021, he was with Huawei Technologies Co., Ltd., Shenzhen, China. From 2021 to 2023, he was with the Department of Electrical Engineering, Shanghai Jiao Tong University, Shanghai, China, as a Postdoctoral Researcher. In September 2023, he joined Shenzhen Institute for Advanced Study, University of Electronic Science and Technology of China as an Associate Researcher. His current research interests include wireless power transfer and solid-state transformers.

Zewei Shen (Member, IEEE) was born in Hubei, China. He received the B.S. degree in control science and engineering and the Ph.D. degree in electrical engineering both from Huazhong University of Science and Technology, Wuhan, China, 2012 and 2020, respectively.

From 2020, he was a Postdoctoral Research Fellow with the School of Automation Engineering, University of Electronic Science and Technology of China (UESTC), Chengdu, China, and Shenzhen Institute for Advanced Study, UESTC. Since September 2022, he has been with the UESTC as a Lecturer. His research interests include electromagnetic interference, high power density power supply, and electric motor drives.

Jianxiao Zou (Member, IEEE) received the B.S., M.S., and Ph.D. degrees in control science and engineering from the University of Electronic Science and Technology of China (UESTC), Chengdu, China, in 2000, 2003, and 2009, respectively.

He is currently a Professor with UESTC, and has been the Vice Dean of Shenzhen Institute for Advanced Study, UESTC, since 2020. He was a Visiting Scholar with the University of California, Berkeley, CA, USA, in 2010, and a Senior Visiting Professor at Rutgers, the State University of New Jersey, New Brunswick, NJ, USA, in 2014. His current research interests include control theory and control engineering, renewable energy control technologies, and intelligent information processing and control.